

Ni–In Intermetallic Nanocrystals as Efficient Catalysts toward Unsaturated Aldehydes Hydrogenation

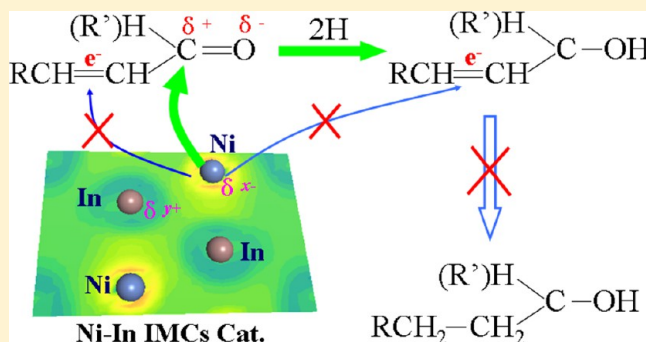
Changming Li, Yudi Chen, Shitong Zhang, Simin Xu, Junyao Zhou, Fei Wang, Min Wei,* David G. Evans, and Xue Duan

State Key Laboratory of Chemical Resource Engineering, Beijing University of Chemical Technology, Beijing 100029, P. R. China

Supporting Information

ABSTRACT: The chemoselective hydrogenation of unsaturated carbonyl compounds is one of the most important and challenging chemical processes in the fine chemical synthesis field, where intermetallic compounds (IMCs) have attracted extensive interest as efficient catalysts. In this work, we demonstrate the preparation of several Ni–In IMCs (Ni_3In , Ni_2In , NiIn , and Ni_2In_3) with a tunable particle size via the utilization of layered double hydroxides (LDHs) precursors that exhibit largely enhanced catalytic activity and selectivity toward the hydrogenation of α,β -unsaturated aldehydes. H_2 -TPR and semi-in situ XRD measurements reveal a coreduction process in the topotactic transformation of NiIn -LDHs materials to Ni–In IMCs. The catalytic behavior toward various unsaturated carbonyl compounds (e.g., furfural, 1-phenyltanol, crotonaldehyde, and 2-hexenal) can be improved by the modulation of the Ni/In ratio and the particle size of these Ni–In IMCs. For instance, a yield of 99% for the hydrogenation of furfural to furfuryl alcohol was obtained over supported Ni_2In catalyst (particle size 5.1 nm, 110 °C, 3 MPa, 2 h). The XAFS characterization and DFT calculation further reveal the electron transfer and active-site isolation in Ni–In IMCs, accounting for the largely enhanced hydrogenation selectivity. The control over the activity and selectivity of Ni–In IMCs catalysts makes them promising candidates for the chemoselective hydrogenation of unsaturated carbonyl compounds.

KEYWORDS: *NiIn*, intermetallic compounds, selective hydrogenation, LDHs



1. INTRODUCTION

Intermetallic compounds (IMCs), which are composed of two or more elements with a specific composition and definite crystal structure, have been used in a variety of applications, including superconductors,¹ magnets,² shape memory alloys,³ and hydrogen storage materials.⁴ Specially, their fascinating catalytic properties have attracted extensive research interests, for instance, the hydrogenation of acetylene on AlFe , PdGa , or RhBi IMCs,⁵ the hydrogenation of unsaturated aldehydes on RuTi or NiSn IMCs,⁶ methanol synthesis and methanol steam reforming on PdGa and PdZn IMCs,⁷ and fuel electrocatalytic oxidation by Pt_3Ti or PtPb IMCs.⁸ However, rigorous preparation conditions are generally required (e.g., high-temperature solid-state reaction) to obtain IMCs, and it is rather difficult to control the structural and morphological homogeneity, which has a significant impact on the resulting catalytic behavior of the IMCs. Although much effort has been made (e.g., physical strategies (CVD),⁹ chemical colloidal synthesis,^{5b,c} or microwave synthesis¹⁰) to solve this problem, these methods still suffer from having an expensive installation, high toxicity, or laborious synthesis process. Therefore, it is highly essential to develop facile and green strategies for the preparation of IMCs as efficient catalysts.

The preferential hydrogenation of the $\text{C}=\text{O}$ group in α,β -unsaturated aldehydes for the production of unsaturated alcohols is one of the most important and challenging chemical processes in the fine chemical synthesis field.^{6,11} Conventional hydrogenation catalysts based on noble or transition metals (e.g., Ru , Pt , Rh , Cu , or Ni) are highly active, but they face the problem of poor selectivity toward unsaturated alcohols because of the kinetically and thermodynamically favored hydrogenation of the $\text{C}=\text{C}$ bond instead of the $\text{C}=\text{O}$ bond. One of the most effective ways to overcome this is to incorporate a second more electropositive metal (e.g., Sn , Ti , or Si) for better catalytic selectivity through the geometric and/or electronic effect, especially in the case of the formation of IMCs.^{6,12} The strong interaction between the component elements in IMCs enables the polarization of the $\text{C}=\text{O}$ group, facilitating its hydrogenation.^{12e,13} Previous work demonstrated that the formation of IMCs (e.g., Ru-Sn ,^{12e} Ru-Ti ,^{6a} Ni-Sn ,^{6b} or Ni-Si ¹⁴ systems) improves the hydrogenation selectivity of some unsaturated aldehydes/ketones, but the hydrogenation activity may decrease significantly as a result of the introduction

Received: July 3, 2013

Revised: September 5, 2013

Published: September 6, 2013



of the second metal. In addition, difficulties in controlling the phase purity, particle size, and uniform morphology of intermetallics lead to unexpected catalytic behavior and obscure structure–function correlation. Therefore, the design and preparation of new IMC catalysts toward the hydrogenation of α,β -unsaturated aldehydes with excellent selectivity and desirable activity remains a challenging goal.

Layered double hydroxides (LDHs) are a class of naturally occurring and synthetic materials generally expressed by the formula $[M^{2+}_{1-x}M^{3+}_x(OH)_2](A^{n-})_{x/n} \cdot mH_2O$ in which the M^{II} and M^{III} cations disperse in an ordered and uniform manner in brucitelike layers.¹⁵ Recently, considerable interest has been focused on LDH materials as heterogeneous catalysts based on their versatility in chemical composition and structural architecture.¹⁶ In particular, a topotactic transformation of LDH materials to uniformly dispersed metal/metal-oxide composites occurs upon calcination in a reductive atmosphere.¹⁷ Inspired by the structural merits of LDH materials, we explored the idea of the incorporation of highly active but minimally selective nickel (Ni) and inactive but more electropositive indium (In) species into the LDH precursor on the atomic scale to fabricate various Ni–In IMCs (e.g., Ni_3In , Ni_2In , $NiIn$, and Ni_2In_3) catalysts toward the selective hydrogenation of α,β -unsaturated aldehydes. The resulting catalysts would possess the following desirable features: first, the atom-scale interspersions of the Ni and In species in the LDH precursor would facilitate the kinetically favored generation of IMCs under moderate reduction conditions and thus guarantee a high dispersion of Ni–In IMCs nanoparticles and second, the versatility in chemical composition of LDHs makes it possible to achieve various single-phase Ni–In IMCs with a tunable ratio. Our approach holds significant promise for Ni–In IMCs as new efficient catalysts toward the selective hydrogenation of α,β -unsaturated aldehydes.

2. EXPERIMENTAL SECTION

2.1. Materials. Indium(III) nitrate hydrate ($In(NO_3)_3 \cdot 36 wt \% In$) was purchased from Sigma-Aldrich. The following analytical-grade inorganic chemicals were used without further purification: NaOH, Na_2CO_3 , $Ni(NO_3)_2 \cdot 6H_2O$, $Mg(NO_3)_2 \cdot 6H_2O$, and $Al(NO_3)_3 \cdot 9H_2O$. Deionized water was used in all of the experimental processes. All organic chemical compounds were purified using standard procedures prior to use.

2.2. Synthesis of the LDHs Precursors and Ni–In IMCs.
Synthesis of the Ni_xIn_y -LDHs and $Ni_xMg_yIn_z$ -LDHs Precursors. The Ni_xIn_y -LDHs with different Ni/In molar ratios (denoted as Ni_3In -LDHs, Ni_2In -LDHs, $NiIn$ -LDHs, and Ni_2In_3 -LDHs) were synthesized by a coprecipitation method. Typically, $Ni(NO_3)_2 \cdot 6H_2O$ and $In(NO_3)_3$ with different molar ratios of Ni^{2+}/In^{3+} were dissolved in 100 mL of deionized water to give a solution with a total cationic concentration of 0.15 M (solution A). A certain amount of NaOH and Na_2CO_3 were dissolved together to obtain 100 mL of a base solution (solution B, $[CO_3^{2-}] = 2.0[M^{3+}]$, $[OH^-] = 1.8([M^{2+}] + [M^{3+}])$). Solutions A and B were then mixed together at a steady rate of 3000 rpm for 1 min. The resulting suspension was aged in a sealed Teflon autoclave at 125 °C for 24 h. The $Ni_xMg_yIn_z$ -LDHs were also synthesized through the same process as the $NiIn$ -LDHs. All of the obtained precipitate was washed thoroughly with water and dried in an oven at 60 °C overnight.

Synthesis of the Ni_3AlIn -LDHs and Ni_2AlIn -LDHs Precursors. Because the coprecipitation method using NaOH and Na_2CO_3 as precipitators results in an impurity phase $In(OH)_3$ in the Al-containing LDHs materials, urea was used in this case. In brief, for the synthesis of Ni_3AlIn -LDHs, $Ni(NO_3)_2 \cdot 6H_2O$, $In(NO_3)_3$, $Al(NO_3)_3 \cdot 9H_2O$, and urea were dissolved in 100 mL of deionized water to give a transparent solution with a concentration of 0.15, 0.05, 0.05, and 2.5 M,

respectively. The resulting solution was aged in a sealed Teflon autoclave at 110 °C for 12 h. The Ni_2AlIn -LDHs were also synthesized through the same process as the Ni_3AlIn -LDHs, with a $Ni(NO_3)_2 \cdot 6H_2O$ concentration of 0.10 M. The obtained precipitate was also washed thoroughly with water and dried in an oven at 60 °C overnight.

Synthesis of Ni–In IMCs. Various unsupported or supported Ni–In IMCs were obtained via an in situ reduction process of the LDHs precursors. In a typical procedure, 1.0 g of LDHs was reduced in a H_2/N_2 (50/50, v/v) stream at different reduction temperatures (from 400 to 900 °C) for 5 h, with an initial heating rate of 2 °C/min. The reduction process results in the phase transformation from LDHs to Ni–In IMCs. The resulting products were slowly cooled to room temperature in a N_2 stream for the subsequent catalytic evaluation.

2.3. Catalytic Evaluation toward the Selective Hydrogenation of Unsaturated Aldehydes. Catalyst, unsaturated carbonyl compounds (1 mL), and *i*-PrOH (30 mL) as the solvent were placed into a stainless steel reaction reactor that was fitted inside a Teflon tank. The air in the vessel was replaced by 3.5 MPa of hydrogen three times and the vessel was then vented and sealed. After the reactor temperature was increased to the target temperature (e.g., 110 °C), H_2 was introduced into the reactor with an initial pressure of 3.0 MPa. After a given reaction time, the activity and selectivity were determined via GC or GC–MS analysis.

2.4. Characterization. Hydrogen temperature programmed reduction (H_2 -TPR) was conducted in a quartz tube reactor on a Micromeritics ChemiSorb 2720 with a thermal conductivity detector (TCD). In each case, the sample (100 mg) was sealed and pretreated at 200 °C in a N_2 atmosphere for 2 h in the reactor, and a gaseous mixture of H_2 and Ar (1:9, v/v) was then fed into the reactor at 40 mL/min. The temperature was raised to 1000 °C at a heating rate of 10 °C/min. Semi-in situ XRD measurements were performed with the following steps: (1) 0.1 g of sample was loaded and in situ reduced in the TPR U-bend to a target temperature (e.g., 400 °C) at a heating rate of 10 °C/min, (2) once the target temperature was achieved, the H_2 was replaced by inert N_2 to stop the reduction reaction immediately, (3) decrease the sample temperature as soon as possible, avoiding structural damage during the cooling process, and (4) the product obtained in the TPR U-bend was placed at room temperature for 2 h followed by XRD measurement.

Powder XRD measurements were performed on a Rigaku XRD-6000 diffractometer using $Cu K\alpha$ radiation ($\lambda = 0.15418$ nm) at 40 kV and 40 mA, with a scanning rate of 10°/min and a 2θ angle ranging from 3° to 90°. The Ni K-edge XAFS measurements were performed at the beamline 1W1B of the Beijing Synchrotron Radiation Facility (BSRF) at the Institute of High Energy Physics (IHEP), Chinese Academy of Sciences (CAS). The element content in the samples was determined by ICP-AES (Shimadzu ICPS-7500). The morphology of the samples was investigated using a Zeiss Supra 55 scanning electron microscope (SEM) with an accelerating voltage of 20 kV combined with energy dispersive X-ray spectroscopy (EDS) for the determination of the metal composition. Transmission electron microscopy (TEM) images were recorded with JEOL JEM-2010 high-resolution transmission electron microscopes. The accelerating voltage was 200 kV. The reaction product was analyzed off-line by a gas chromatograph (GC, Shimadzu, 2014C) equipped with a flame ionization detector (FID) or by gas chromatography–mass spectrometry (GC–MS, Shimadzu, 2010). The specific surface area measurements were performed on the basis of the Brunauer–Emmett–Teller (BET) method using a Quantachrome Autosorb-1C-VP analyzer.

3. COMPUTATIONAL METHODS

All calculations were performed with the periodic density functional theory (DFT) method using Dmol3 module in the Material Studio 5.5 software package (Accelrys Inc., San, Diego, CA).¹⁸ The single-crystal cell structural models for Ni_3In , Ni_2In , $NiIn$, and Ni_2In_3 were built according to previous reports¹⁹ in which the crystal structure is the same as that from our experimental results: Ni_3In , $P63/mmc$; Ni_2In , $P63/mmc$; $NiIn$, $P6/mmm$; and Ni_2In_3 , $P\bar{3}m1$ (for details, see the Supporting Information). The generalized gradient approximation

(GGA) with the Perdew–Burke–Ernzerhof (PBE)²⁰ functional and effective core potentials with double-numeric quality basis were utilized for the geometric optimization and single-point energy calculations. During the calculations, the convergence tolerance was set as follows: energy = 1.0×10^{-6} Ha, force = 1.0×10^{-3} Ha/Å, and displacement = 1.0×10^{-3} Å.

4. RESULTS AND DISCUSSION

4.1. Structure and Morphology of Unsupported Ni_xIn_y IMCs. Binary Ni_xIn_y-LDHs precursors were successfully prepared by the coprecipitation method. Figure 1 shows the

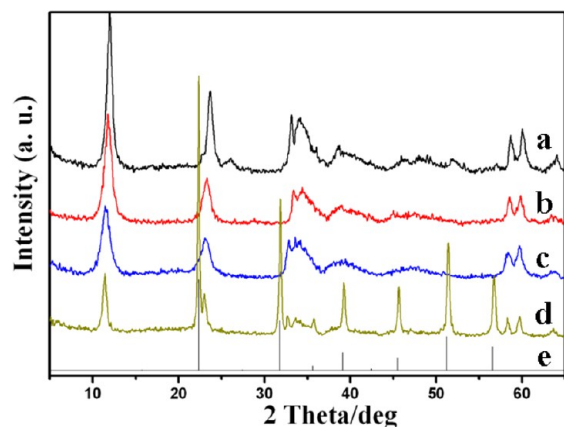


Figure 1. XRD patterns of the as-synthesized Ni_xIn_y-LDHs with various ratios of $x(\text{Ni}):y(\text{In})$: (a) 3:1, (b) 2:1, (c) 1:1, and (d) 2:3, respectively. (e) XRD standard card of In(OH)₃ (JCPDS 16-0161).

XRD patterns of Ni_xIn_y-LDHs with various Ni/In ratios, all of which can be indexed as a rhombohedral structure with the typical (003), (006), (110), and (113) reflections at 2θ 11.95°, 23.70°, 58.61°, and 60.05° for LDHs materials, respectively. No other crystalline phase was detected for Ni_xIn_y-LDHs with a Ni/In ratio ≥ 1 (Figure 1a–c), indicating the high purity of these LDHs materials. The reflection intensity decreases gradually from curve a to c, indicating the crystallinity decline of the Ni_xIn_y-LDHs phase with the decrease of the Ni/In ratio. In the case of Ni₂In₃-LDHs (Figure 1d), however, the impurity of In(OH)₃ was observed besides the LDHs phase in comparison with the JCPDS for In(OH)₃ (Figure 1e). The results are consistent with the empirical rule for the formation of LDHs materials (i.e., the M^{2+}/M^{3+} ratio < 1 in the feed intake does not guarantee a pure LDHs phase).²¹ Figure 2 shows SEM images of these Ni_xIn_y-LDHs precursors. Both the Ni₃In-LDH and Ni₂In-LDHs precursors (Figure 2A,B) display a typical hexagonal nanoplatelet morphology with diameter of 50–100 nm, indicating their good crystallization. For NiIn-LDHs (Figure 2C), the nanoplatelets become irregular and inconstant, which is in accordance with the reduced XRD intensity (Figure 1c). In the case of the impure Ni₂In₃-LDH precursor, however, some cubic nanocrystals were also observed besides the nanoplatelets (Figure 2D), which can be attributed to the In(OH)₃ phase indicated by its XRD pattern (Figure 1d).

After the in situ reduction process in the hydrogen atmosphere, the Ni_xIn_y-LDHs precursors transformed to corresponding single intermetallic phases Ni₃In, Ni₂In, NiIn, and Ni₂In₃ IMCs, respectively, as shown in Figure 3. It is observed that the XRD patterns of the as-synthesized Ni–In IMCs are well consistent with their corresponding XRD standard cards, indicating the successful synthesis of pure Ni–

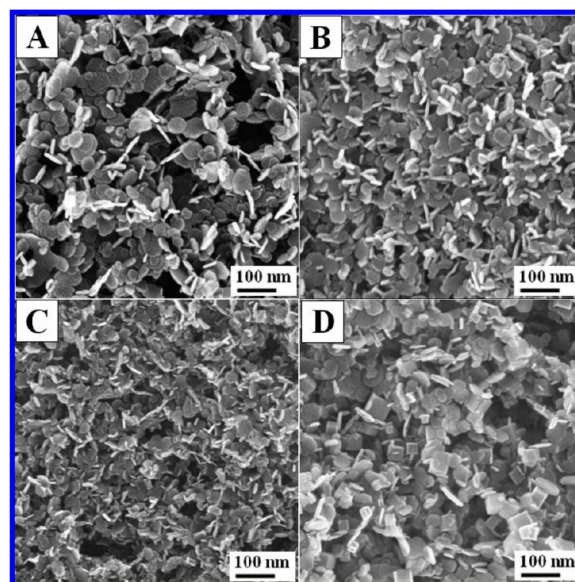


Figure 2. SEM images of the as-synthesized Ni_xIn_y-LDHs with various ratios of $x(\text{Ni}):y(\text{In})$: (A) 3:1, (B) 2:1, (C) 1:1, and (D) 2:3, respectively.

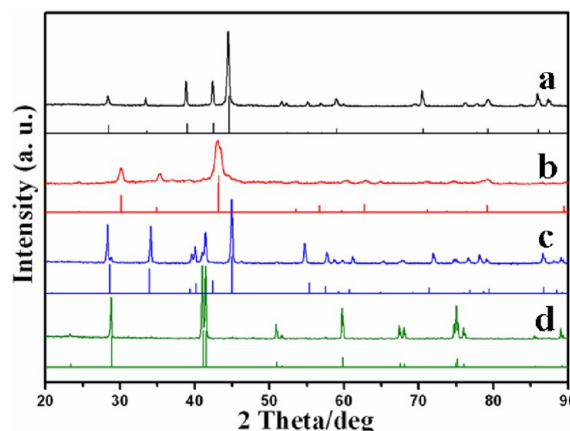


Figure 3. XRD patterns of the unsupported Ni–In IMCs derived from the in situ reduction of the Ni_xIn_y-LDHs precursors: (a) Ni₃In at 400 °C, (b) Ni₂In at 400 °C, (c) NiIn at 400 °C, and (d) Ni₂In₃ at 600 °C. The XRD standard cards for the corresponding Ni–In IMCs are shown in the lower part of the panels: Ni₃In–PDF#65-3522, Ni₂In–PDF#65-3486, NiIn–PDF#07-0178, and Ni₂In₃–PDF#65-3486.

In IMCs by the utilization of the versatility in the chemical composition of the LDHs precursors. It is worth noting that the pure Ni₂In₃ IMC can be only obtained at a reduction temperature as high as 600 °C owing to the impurity of its LDHs precursor, whereas the other three (Ni₃In, Ni₂In and NiIn) IMCs were obtained at a low reduction temperature of 400 °C. For the Ni₂In₃ IMC, the reduction at 400 °C results in both NiIn and Ni₂In₃ IMC phases (Figure S1) that is probably due to the incomplete reduction of In species, which will be further elaborated in the following section.

The morphology and structural features of the Ni–In IMCs after the in situ reduction process were further revealed by SEM and TEM (Figure 4). The in situ reduction leads to the transformation of the LDHs samples to their corresponding Ni–In IMCs. It can be seen that the original platelike morphology of LDH nanocrystals was thoroughly collapsed

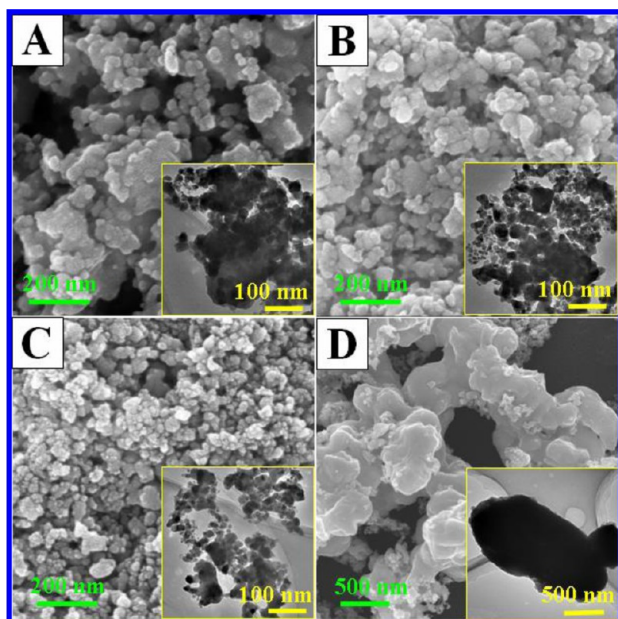


Figure 4. SEM images of the unsupported Ni–In IMCs derived from the in situ reduction of the Ni_xIn_y -LDHs precursors: (a) Ni_3In at 400 °C, (b) Ni_2In at 400 °C, (c) $NiIn$ at 400 °C, and (d) Ni_2In_3 at 600 °C. The insets show their corresponding TEM images.

to form irregular particles with a wide size distribution (50–300 nm) for Ni_3In , Ni_2In , and $NiIn$ IMCs (Figure 4A–C). For the Ni_2In_3 IMC sample (Figure 4D), serious aggregation was observed with much larger particle size even to several micrometers, owing to the higher reduction temperature (600 °C).

4.2. Fabrication of Supported Ni–In IMCs with Tunable Particle Size. In the Results and Discussion, section 4.1, several homogeneous Ni–In IMCs derived from Ni_xIn_y -LDHs precursors have been obtained, but their particle size can not be easily tuned. The large particle size of Ni–In IMCs may result in unsatisfactory catalytic activity owing to the low specific surface area. In this part, we further utilize the constituent diversity of LDHs to prepare ternary $Ni_xAl_yIn_z$ -LDHs or $Ni_xMg_yIn_z$ -LDHs precursors by the introduction of the Al or Mg element in the LDH precursors for the purpose of fabricating supported Ni–In IMCs with tunable particle size by a similar reduction process. Taking Ni_2AlIn -LDHs and $Ni_2Mg_7In_3$ -LDHs as examples, the XRD patterns confirm the successful synthesis of precursors with typical reflections for LDHs materials (Figure 5A). The small difference in the 2θ reflections between the two LDHs precursors is due to their different metal proportions and ionic radii. After the subsequent in situ reduction process in a hydrogen atmosphere (400 °C), the supported Ni_2In IMC in Al_2O_3 matrix (Ni_2In/Al_2O_3) as well as the Ni_2In_3 IMC in MgO matrix ($Ni_2In_3/7MgO$) was obtained whose XRD patterns (Figure 5B) display a high purity of the Ni_2In and Ni_2In_3 phase, respectively. The notable reduced full-width at half-maximum (fwhm) in the XRD reflection for Ni_2In and Ni_2In_3 IMCs in comparison with their unsupported counterparts (Figure 3b,d) indicates the significantly decreased particle size. The characteristic reflections of a MgO phase were also observed in the $Ni_2In_3/7MgO$ sample, but no Al_2O_3 phase was detected in the sample of Ni_2In/Al_2O_3 , suggesting crystalline MgO and amorphous Al_2O_3 in the $Ni_2In_3/7MgO$ and Ni_2In/Al_2O_3 samples, respectively.

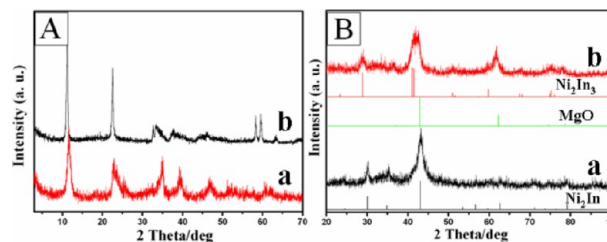


Figure 5. (A) XRD patterns of the typical ternary LDHs precursors: (a) Ni_2AlIn -LDHs and (b) $Ni_2Mg_7In_3$ -LDHs. (B) XRD patterns of the resulting supported Ni–In IMCs: (a) Ni_2In/Al_2O_3 and (b) $Ni_2In_3/7MgO$. The XRD standard cards for Ni_2In , Ni_2In_3 , and MgO are also shown in the lower part of the panels, as noted in panel B: Ni_2In -PDF#65-3486, Ni_2In_3 -PDF#65-3486, and MgO-PDF#45-0946.

The SEM images in Figure 6 show the morphology of the ternary LDHs precursors and the corresponding supported

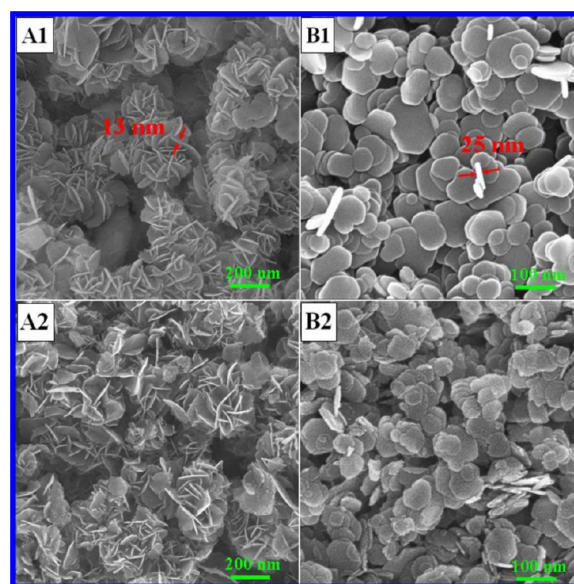


Figure 6. SEM images of the typical ternary LDHs precursors: (A1) Ni_2AlIn -LDHs and (B1) $Ni_2Mg_7In_3$ -LDHs and their resulting supported Ni–In IMCs after in situ reduction, (A2) Ni_2In/Al_2O_3 and (B2) $Ni_2In_3/7MgO$.

Ni–In IMCs after the in situ reduction process. It is very interesting to see that for the sample of Ni_2AlIn -LDHs, a flowerlike hierarchical morphology was observed that is composed of numerous nanoplatelets (diameter, 100–200 nm; thickness, ~13 nm) (Figure 6A1). Furthermore, the mother morphology is still maintained in the resulting supported Ni_2In/Al_2O_3 product after the reduction process (Figure 6A2), indicating the mechanical stability of the sample. In the case of the $Ni_2Mg_7In_3$ -LDHs sample, individual nanoplatelets (diameter, 50–200 nm; thickness, ~25 nm) were observed (Figure 6B1). The reduction product $Ni_2In_3/7MgO$ also inherits the original flake morphology, except for a little shrinking in the particle size (Figure 6B2).

The structure of the two supported Ni–In IMCs was further investigated by TEM (Figure 7). It is observed from the low-magnification TEM images (Figure 7A1,B1) that the Ni_2In/Al_2O_3 and $Ni_2In_3/7MgO$ samples maintain the flowerlike and flakelike morphology of their mother LDHs precursors, respectively. Moreover, numerous uniform and highly dispersed

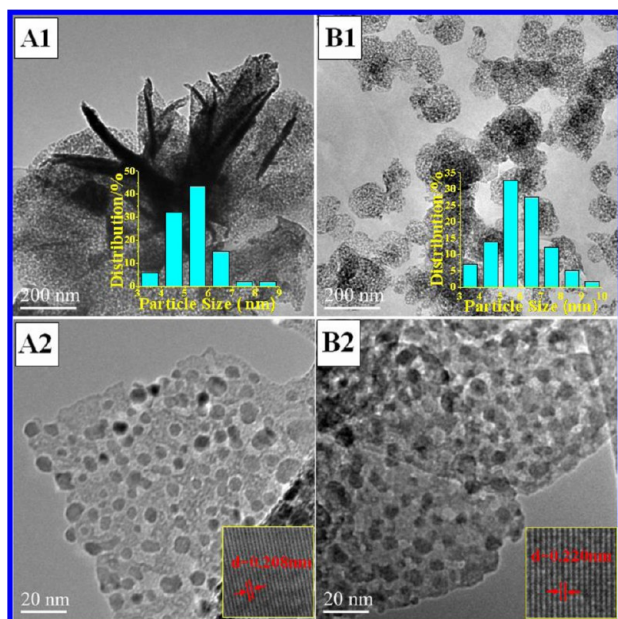


Figure 7. TEM images of supported Ni–In IMCs: (A1) low- and (A2) high-magnification image for $\text{Ni}_2\text{In}/\text{Al}_2\text{O}_3$ and (B1) low- and (B2) high-magnification image for $\text{Ni}_2\text{In}_3/7\text{MgO}$. The insets show the size distribution (panels A1 and B1) and the HRTEM lattice fringe (panels A2 and B2) for the Ni_2In and Ni_2In_3 nanoparticles, respectively.

small dots in the matrix were observed for the two samples. The HRTEM images (Figure 7A2,B2) further reveal the supported Ni_2In and Ni_2In_3 nanoparticles, with an average diameter of 5.1 and 5.9 nm (measured on the basis of 200 particles), respectively. The single crystalline nature of Ni_2In and Ni_2In_3 was observed by the HRTEM images (Figure 7A2,B2 inset). The lattice spacings of 0.208 and 0.220 nm are attributed to the (102) plane of hexagonal $P6_3/mmc$ (194) Ni_2In and the (110) plane of $P\bar{3}m1$ (164) Ni_2In_3 , respectively. This is in good accordance with the XRD results in Figure 5B. On the basis of the results of the XRD, SEM, and TEM, the introduction of the inert Al or Mg element into the LDHs matrix maintains the structural features during the topotactic transformation and facilitates the generation of highly dispersed supported Ni–In IMCs.

In addition, the particle size of the supported Ni_2In_3 IMC can be tuned by changing the Mg content in the LDHs precursor. Figure S2 shows the successful synthesis of the $\text{Ni}_2\text{Mg}_x\text{In}_3$ -LDHs precursors with various Mg content: $\text{Ni}_2\text{Mg}_2\text{In}_3$ -LDHs, $\text{Ni}_2\text{Mg}_4\text{In}_3$ -LDHs, $\text{Ni}_2\text{Mg}_7\text{In}_3$ -LDHs, and $\text{Ni}_2\text{Mg}_{13}\text{In}_3$ -LDHs. The XRD patterns for the reduction products ($\text{Ni}_2\text{In}_3/x\text{MgO}$) of these $\text{Ni}_2\text{Mg}_x\text{In}_3$ -LDHs precursors are displayed in Figure S3. It was observed that as the Mg content increases from $\text{Ni}_2\text{In}_3/2\text{MgO}$ to $\text{Ni}_2\text{In}_3/13\text{MgO}$, the XRD reflections assigned to MgO phase ((200) and (220) at 2θ 42.8° and 62.3°) get stronger, whereas the (101) and (110) reflection at 2θ 28.8° and 41.4° attributed to the Ni_2In_3 phase becomes weaker with a gradually reduced full-width at half-maximum (fwhm), indicating the decreased particle size with the increase of the Mg content. TEM images further reveal the change in particle size of these $\text{Ni}_2\text{In}_3/x\text{MgO}$ products (Figure S4). The mean particle size of supported Ni_2In_3 decreases gradually from 13.8 ($\text{Ni}_2\text{In}_3/2\text{MgO}$, Figure S4A) to 8.7 ($\text{Ni}_2\text{In}_3/4\text{MgO}$, Figure S4B), 5.9 ($\text{Ni}_2\text{In}_3/7\text{MgO}$, Figure S4C), and finally to 4.1 nm ($\text{Ni}_2\text{In}_3/13\text{MgO}$, Figure S4D). It is therefore concluded that

the Mg element serves as a dispersant for the formation of Ni–In IMCs and that the particle size of a supported Ni–In nanocrystal can be facilely tuned by changing the Mg content.

4.3. Topotactic Transformation from LDHs Materials to Ni–In IMCs. The deep insight into the topotactic transformation of LDHs materials to IMCs could help in the controlled synthesis of IMCs and to understand their structural features for further catalytic applications. Hydrogen temperature programmed reaction (H_2 -TPR) measurements were carried out to give key information on the redox properties of the LDH materials. Figure 8A demonstrates the comparative

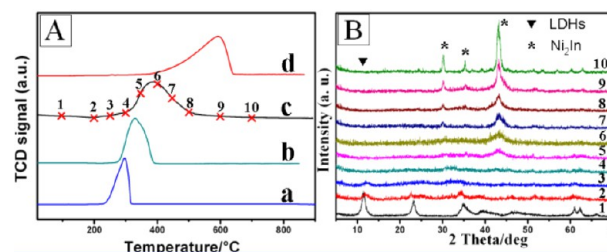


Figure 8. (A) H_2 -TPR profiles of (a) $\text{Ni}(\text{OH})_2$, (b) Ni_2In -LDHs, (c) Ni_2AlIn -LDHs, and (d) $\text{In}(\text{OH})_3$. (B) Semi-in situ XRD patterns of Ni_2AlIn -LDHs captured at different target temperatures from 50 to 700 °C (line 1 to 10), as labeled in panel A.

study of the Ni_2In -LDHs and Ni_2AlIn -LDHs as well as their corresponding individual hydroxides. $\text{Ni}(\text{OH})_2$ and $\text{In}(\text{OH})_3$ exhibit the lowest and highest reduction temperature, with the main peak at 297 and 593 °C, respectively (Figure 7A, curves a and d). Interestingly, the Ni_2In -LDHs sample shows only one reduction peak at 330 °C between that of $\text{Ni}(\text{OH})_2$ and $\text{In}(\text{OH})_3$ (Figure 7A, curve b), indicating the presence of interactions between Ni and In hydroxide in the LDH matrix during the generation of Ni–In IMCs. In the case of the ternary Ni_2AlIn -LDHs by introducing the third component, Al, its reduction temperature was improved to 384 °C (Figure 7A, curve c), which is most probably a result of the segregation effect of the Al element. In any case, an intermediate reduction temperature of the LDHs materials compared with their individual hydroxides reveals that a strong interaction occurs between the nickel and indium building unit that facilitates the reduction process of the indium species. These results can be used to interpret the difficulty in the reduction of the $\text{In}(\text{OH})_3$ -containing impure Ni_2In_3 -LDHs, further indicating the key role of the atom-scale interspersion of Ni and In species in the LDHs precursor for the generation of Ni–In IMCs.

A semi-in situ XRD measurement was performed to discover further the topotactic transformation process of LDHs (for experimental details, see Experimental Section 2.4). Owing to the partial overlapping of the XRD reflections for the Ni–In IMCs and the MgO phase, the Ni_2AlIn -LDHs precursor was chosen as a typical ternary sample instead of the Mg-containing LDHs precursor, avoiding the interference of the strong MgO diffraction peak. The resulting XRD patterns obtained in the temperature range 50–700 °C as labeled in Figure 8Ac are shown in Figure 8B (from line 1 to 10). With the increase of the reduction temperature from 50 to 250 °C, the (003) and (006) reflections of LDHs phase disappears gradually (Figure 8B, line 1 to 3), and an amorphous state was found at 300 °C (Figure 8B, line 4). This corresponds to the absence of any reduction signal (50–300 °C) in the TPR curve (Figure 8A-c). The further elevated temperature over 350 °C resulted in the

appearance of the characteristic reflection at 2θ 43.16° for Ni₂In phase (Figure 8B, line 5), corresponding to the reduction peak at 384 °C in the TPR curve (Figure 8Ac). This process involves the reduction of both the Ni and In species simultaneously to generate Ni₂In IMC. Subsequently, the intensity of the Ni₂In reflection increases gradually from 350 to 500 °C (Figure 8B, line 5 to 8). The further increased temperature from 500 to 700 °C leads to the remarkable particle reunion, indicated by the significantly reduced full-width at half-maximum (fwhm) of the Ni₂In reflections (Figure 8B, line 9 to 10). On the basis of the results of the TPR and semi-in situ XRD, it is concluded that the Ni and In species in the LDH precursor undergo a coreduction process during the topotactic transformation of LDHs to Ni₂In IMC.

4.4. Catalytic Selective Hydrogenation of Various Unsaturated Carbonyl Compounds. The catalytic performances of the as-synthesized supported Ni–In IMCs catalysts were first evaluated by the selective hydrogenation of the typical unsaturated aldehyde furfural to furfuryl alcohol, which is a promising chemical intermediate for the synthesis of biosourced products widely using in the polymer industry.²² As a reference sample, the supported Ni/Al₂O₃ catalyst derived from the Ni₂Al-LDHs precursor was also synthesized by a similar method. The detailed information for these catalysts is summarized in Table S1. Figure 9 demonstrates the catalytic

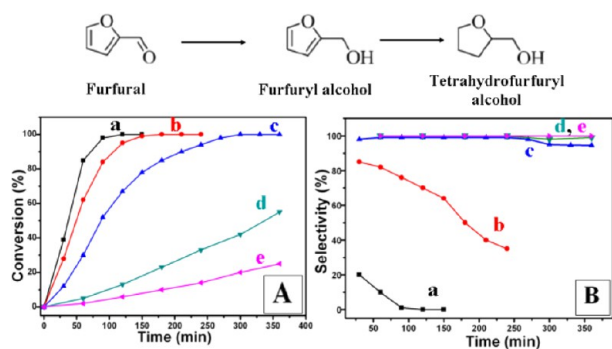


Figure 9. (A) Catalytic conversion and (B) corresponding selectivity for the hydrogenation of furfural to furfuryl alcohol over different catalysts vs reaction time: (a) Ni/Al₂O₃, (b) Ni₃In/Al₂O₃, (c) Ni₂In/Al₂O₃, (d) NiIn/3MgO, and (e) Ni₂In₃/7MgO. The reaction conditions are furfural/Ni ratio = 15; furfural, 1.0 mL; *i*-PrOH, 30 mL; temperature, 110 °C; and H₂ pressure, 3.0 MPa.

conversion and corresponding selectivity for the hydrogenation of furfural over these catalysts versus the reaction time. It is observed that the Ni/Al₂O₃ catalyst shows the best hydrogenation activity but the worst selectivity (Figure 9, curve a), which is consistent with a previous report.^{6b} The catalytic activity decreases generally with the decreased Ni/In ratio in the Ni–In IMCs, with the following order: Ni > Ni₃In > Ni₂In > NiIn > Ni₂In₃. In contrast, the selectivity toward furfuryl alcohol displays an opposite trend, and the best catalytic performance with a 99% furfuryl alcohol yield can be obtained over the Ni₂In/Al₂O₃ catalyst (particle size 5.1 nm) at 110 °C (Figure 9, curve c). Compared with the classical systems used in industry, the catalytic selectivity toward furfuryl alcohol in this work is significantly superior to the Raney Nickel catalyst^{6b} and is comparable to the commercial Cu–Cr catalysts^{22a,23,24} but with a decreased operation temperature (more than 20 °C). Moreover, this catalyst also demonstrates good reusability and durability over five consecutive cycles of use (Table S2); no

obvious phase separation and agglomeration of the Ni₂In nanoparticles are observed in the used Ni₂In/Al₂O₃ catalyst, as indicated by the XRD patterns and TEM image (Figure S5). The excellent catalytic performance of Ni–In IMCs makes them a promising candidate for the selective hydrogenation of furfural.

We further evaluated the selective hydrogenation of other unsaturated carbonyl compounds over these Ni–In IMCs catalysts compared with the monometallic Ni/Al₂O₃ sample. A similar tendency was observed (i.e., for a specific substrate, the catalytic activity decreases gradually along with the enhancement of selectivity in the order of Ni, Ni₃In, Ni₂In, NiIn, and Ni₂In₃). For acetophenone (Table 1, substrate 1), a high selectivity (99%) toward 1-phenylethanol can even be achieved over Ni₃In/Al₂O₃ owing to the relatively stable benzene ring. The selectivity begins to drop over hydrogenation of the weak π – π interaction unsaturated aldehydes such as 3-cyclohexene-1-carboxaldehyde and β -hexenoic aldehyde (Table 1, substrates 2 and 3). In the cases of crotonaldehyde and 2-hexenal (Table 1, substrates 4 and 5), the strong π – π interaction may suppress the hydrogenation reaction. The elevated reaction temperatures for better conversion results in a dramatic loss of selectivity, but good hydrogenation selectivity still can be achieved over the Ni₂In₃/7MgO catalyst. The best product yield of unsaturated alcohols over various Ni–In IMCs can be obtained, as denoted by the blue step in Table 1. In an effort to improve the catalytic behavior of the supported Ni₂In₃ IMC, we further investigated the size effect of Ni₂In₃ on the activity and selectivity toward hydrogenation of 2-hexenal. Figure S6 displays the catalytic activity and corresponding selectivity over Ni₂In₃/*x*MgO catalysts with different particle sizes versus reaction time. It is observed that as the particle size of the supported Ni₂In₃ decreases from 13.8 to 4.1 nm, the catalytic activity increases obviously along with a slightly decreased selectivity toward 2-hexenal. The best yield of 78.8% for 2-hexenal (con. 90.2%, sel. 87.2%) can be obtained over the Ni₂In₃/13MgO catalyst (particle size 4.1 nm). The results demonstrate that the activity and selectivity for hydrogenation of various unsaturated carbonyl compounds can be enhanced via tuning the chemical composition of the Ni–In IMCs and their particle size.

4.5. Geometry and Electronic Structure of the Ni–In IMCs by XAFS and DFT Study. To gain deeper insight into the structure–function correlation, XAFS characterization and DFT calculations were conducted to elucidate the electronic structure and atomic configuration in their local environment for the four Ni–In IMCs. The normalized Ni K-edge X-ray absorption near-edge structure (XANES) spectra of the supported Ni–In IMCs as well as the reference samples of Ni foil and NiO are shown in Figure 10A. It can be observed that all of the Ni–In IMCs samples are more akin to metallic Ni than NiO, suggesting the predominantly metallic state of Ni in Ni–In IMCs. The obvious shift of the absorption edge toward low photon energy relative to the Ni foil reveals the enrichment of electron on the Ni atom (denoted as Ni^{δ-}) in the Ni–In IMCs.^{25,9b} This may result from the electron transfer from the In atom to the Ni atom, which is in accordance with the electronegativity values of In (1.7) and Ni (1.9). Figure 10B shows the Fourier transform of the Ni K-edge EXAFS oscillations in R space. Obviously, the first nearest-neighbor distance for Ni–In IMCs is significantly different from that for Ni foil. As for Ni₃In and Ni₂In IMCs, the first nearest-neighbor distance increases slightly compared with Ni foil. Two main peaks at the first nearest-neighbor distance were even observed

Table 1. Hydrogenation of Unsaturated Carbonyl Compounds and Ketones Catalyzed by Various Supported Ni–In IMCs Catalysts^a

Entry	Substrate	Product	Temp./°C	Ni/Al ₂ O ₃		Ni ₃ In/Al ₂ O ₃		Ni ₂ In/Al ₂ O ₃		NiIn/3MgO		Ni ₂ In ₃ /7MgO	
				Con.	Sel.	Con.	Sel.	Con.	Sel.	Con.	Sel.	Con.	Sel.
1			120	98%	69%	81%	99%	74%	100%	63%	100%	47%	100%
2			120	100%	16%	92%	51%	83%	96%	72%	100%	65%	100%
3			130	100%	12%	89%	43%	76%	87%	68%	98%	54%	100%
4			145	94%	13%	84%	27%	75%	50%	62%	68%	47%	95%
5			145	88%	10%	70%	23%	56%	44%	45%	65%	38%	92%

^aReaction conditions: substrate/Ni = 15; *i*-PrOH, 30 mL; H₂ pressure, 3.0 MPa; reaction time, 2 h. The conversion and selectivity were determined by GC using an internal standard technique.

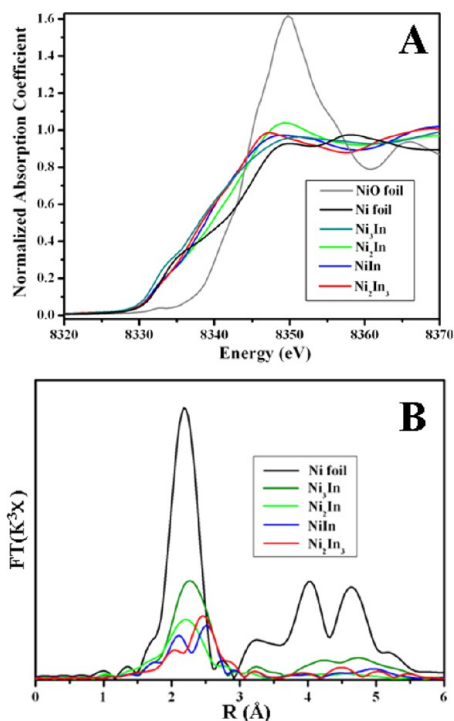


Figure 10. (A) Normalized intensity of the Ni K-edge XANES spectra for the supported Ni–In IMCs, Ni, and NiO. (B) Corresponding Fourier transform k^3 -weighted EXAFS spectra in R space compared with Ni foil.

in the cases of the NiIn and Ni₂In₃ IMCs. The results qualitatively indicate the strong Ni–In interaction in Ni–In IMCs as well as the variation in the chemical bonding or coordination environment.

DFT calculations were further performed to give an understanding of the electron and geometry features of Ni–In IMCs. The structural models for Ni–In IMCs are shown in Figure S7, which were chosen according to the XRD patterns. The electron density difference contour maps (Figure S8) demonstrate the polarization of Ni–In bonding, resulting from the electron transfer from the In atom to the Ni atom,²⁶ which is consistent with the XAFS observations. The total electron density contour maps in Figure S9 further display the increased

partial overlap from Ni₃In to NiIn, indicating the enhanced electron interaction. The calculated specific charge quantity of the Ni atom increases from $-0.088e$ (Ni₃In) to $-0.310e$ (Ni₂In₃) as the Ni/In ratio decreases in these Ni–In IMCs.

Another unique feature of intermetallic compounds is the so-called “active-site isolation” as proposed by Robert Schlögl’s group.²⁷ For Ni–In IMCs, the transition metal Ni is the active component, whereas In is inert in the catalytic hydrogenation reaction. To identify the isolation effect, the high-angle annular dark-field micrographs (HAADF-STEM) and the corresponding energy-dispersive spectroscopy mapping analysis (STEM-EDS) were performed for the typical Ni₂In/Al₂O₃ sample, as shown in Figure S10. It can be observed that both the Ni and In elements are distributed homogeneously in the same Ni₂In nanoparticle, indicating the isolation effect. In addition, the site isolation of active Ni by the inactive In element in Ni–In IMCs is clearly demonstrated by the DFT simulation (Figure 11). The decreased Ni–Ni coordination was observed with the increase of the In/Ni ratio. Specifically, the Ni atoms were completely isolated by In atoms in the Ni₂In₃ (110) face. The active-site isolation imposes great influence on the adsorption property of Ni–In IMCs, such as the adsorption of the H atom

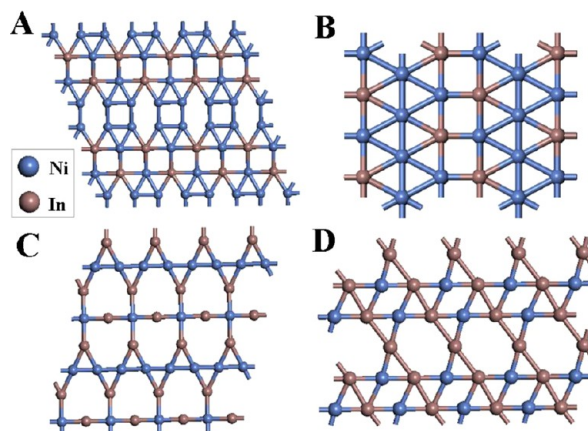
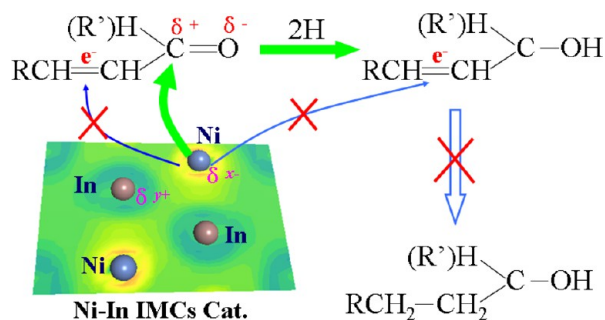


Figure 11. Atomic arrangement and chemical bonding of the preferential crystal face of Ni–In IMCs (according to XRD diffraction): (A) Ni₃In (201) face, (B) Ni₂In (110) face, (C) NiIn (201) face, and (D) Ni₂In₃ (110) face.

on the (201) plane of Ni₂In in Figure S11. Interestingly, wherever the initial H atom was placed (center site and top site of the In atom or top site of the Ni atom), it was preferentially located at the hole site of Ni with a slight structural reconfiguration of the surface Ni and In atoms. The results indicate that the site isolation of Ni by In may deactivate partial adsorption sites toward the H atom.

The observed electron transfer and active-site isolation in the Ni–In IMCs have a great impact on their catalytic performance (shown in Scheme 1). It is well-known that hydrogenation of

Scheme 1. Schematic Illustration of the Reaction Path for the Selective Hydrogenation of Unsaturated Carbonyl Compounds over the Ni–In IMC Catalysts



carbonyl (C=O) and alkenyl (C=C) follow the nucleophilic and electrophilic addition mechanism, respectively. For the adsorption of carbonyl (C=O) on metal, three adsorption states (on-top η_1 , di- σ_{CO} η_2 , and π_{CO} η_2) have been reported (see Figure S12 for details).²⁸ In this work, the adsorption of the C=O group via the di- σ_{CO} η_2 form is rather possible owing to the charge matching between the C=O group and Ni–In bonding. The electronegative Ni atom in Ni–In IMCs catalysts prefers to attack the positively charged carbon terminal of carbonyl instead of the electron-rich alkenyl. Moreover, active-site isolation in Ni–In IMCs may decrease the adsorption of the alkenyl (C=C)^{27,29} and H atom, thereby blocking the hydrogenation of the alkenyl (C=C) group. The preferential hydrogenation of the carbonyl (C=O) accounts for the increased hydrogenation selectivity toward the unsaturated alcohol over Ni–In IMCs. However, the electron transfer from In to Ni could occupy the partially vacant d-electron orbital of the Ni atom,³⁰ which may damage its adsorption and reactivity capability and therefore decrease the hydrogenation activity. This agrees well with the experimental tendency of the catalytic activity and selectivity in the hydrogenation of unsaturated carbonyl compounds over various Ni–In IMCs: the decrease of the Ni/In ratio leads to depressed catalytic activity but enhanced selectivity.

5. CONCLUSIONS

We have developed a facile methodology for the preparation of highly dispersed Ni–In IMCs (Ni₃In, Ni₂In, NiIn, and Ni₂In₃) nanoparticles with a tunable size based on an LDH approach, and we have demonstrated their effective catalytic behavior toward the selective hydrogenation of various unsaturated aldehydes. The LDH precursor plays a key role in the synthesis of supported Ni–In IMCs: the LDHs versatility in chemical composition as well as the atom-scale interspersions of components in LDHs facilitate the formation of highly dispersed Ni–In IMCs with a tunable particle size. The

catalytic evaluations show that these supported Ni–In IMCs exhibit excellent catalytic activity and selectivity toward the hydrogenation of unsaturated carbonyl compounds (e.g., furfural, 1-phenyl ethanol, crotonaldehyde, and 2-hexenal) by the modulation of the chemical composition and particle size of Ni–In IMCs. XAFS characterization and DFT calculation further reveal the electron transfer from the In atom to the Ni atom as well as active-site isolation, which favors the nucleophilic addition process of a C=O group instead of the electrophilic addition of C=C, accounting for the largely enhanced hydrogenation selectivity over Ni–In IMCs. The control over the composition and morphology of Ni–In IMCs demonstrated in this work makes them a promising candidate toward the chemoselective hydrogenation of unsaturated carbonyl compounds.

■ ASSOCIATED CONTENT

Supporting Information

XRD pattern of the sample derived from the in situ reduction of the Ni₂In₃-LDHs precursor at 400 °C, XRD patterns of the as-synthesized Ni₂Mg_xIn₃-LDHs with different Mg content, XRD patterns of the supported Ni₂In₃/xMgO derived from the in situ reduction of the Ni₂Mg_xIn₃-LDHs precursors with different Mg content, TEM images and particle size distribution of the supported Ni₂In₃/xMgO derived from the in situ reduction of the Ni₂Mg_xIn₃-LDHs precursors with different Mg content, detailed information for the samples used as a hydrogenation catalyst, recycling results of the selective hydrogenation of furfural to furfural alcohol over Ni₂In/Al₂O₃ catalyst, XRD patterns of the used Ni₂In/Al₂O₃ catalyst after five consecutive cycles compared with the fresh Ni₂In/Al₂O₃ catalyst, TEM image of the used Ni₂In/Al₂O₃ catalyst, size effect on the activity and selectivity for hydrogenation of 2-hexenal to 2-hexenol over Ni₂In₃/xMgO catalysts with different particle size, single-crystal-cell structural models for Ni–In IMCs after geometry optimization, DFT results for the electron density difference contour maps of Ni–In IMCs, DFT results for the total electron density contour maps of Ni–In IMCs, STEM image of the Ni₂In/Al₂O₃ sample accompanied by EDS mapping of Ni and In for one nanoparticle, simulative adsorption of the H atom on the Ni₂In (201) plane, three adsorbed states of the C=O group in α,β -unsaturated aldehydes on Pt or Pd surfaces (PDF). This material is available free of charge via the Internet at <http://pubs.acs.org>.

■ AUTHOR INFORMATION

Corresponding Author

*E-mail: weimin@mail.buct.edu.cn.

Notes

The authors declare no competing financial interest.

■ ACKNOWLEDGMENTS

This work was supported by the 973 Program (grant no. 2011CBA00504), the National Natural Science Foundation of China (NSFC). M.W. particularly appreciates the financial aid from the China National Funds for Distinguished Young Scientists of the NSFC.

■ REFERENCES

- (1) (a) Cava, R. J.; Zandbergen, H. W.; Krajewski, J. J.; Peck, W. F.; Siegriest, T.; Batlogg, B.; Vandover, R. B.; Felder, R. J.; Mizuhashi, K.; Lee, J. O.; Eisaki, H.; Uchida, S. *Nature* **1994**, *367*, 252. (b) He, T.; Huang, Q.; Ramirez, A. P.; Wang, Y.; Regan, K. A.; Rogado, N.;

- Hayward, M. A.; Haas, M. K.; Slusky, J. S.; Inumara, K.; Zandbergen, H. W.; Ong, N. P.; Cava, R. J. *Nature* **2001**, *411*, 54.
- (2) (a) Sun, S.; Murray, C. B.; Weller, D.; Folks, L.; Moser, A. *Science* **2000**, *287*, 1989. (b) Sun, S. *Adv. Mater.* **2006**, *18*, 393.
- (3) (a) Wuttig, M.; Liu, L.; Tsuchiya, K.; James, R. D. *J. Appl. Phys.* **2000**, *87*, 4707. (b) Otsuka, K.; Ren, X. B. *Intermetallics* **1999**, *7*, 511.
- (c) Cable, R. E.; Schaak, R. E. *Chem. Mater.* **2007**, *19*, 4098.
- (4) (a) Bououdina, M.; Grant, D.; Walker, G. *Int. J. Hydrogen Energy* **2006**, *31*, 177. (b) Cohen, R. L.; Wernick, J. H. *Science* **1981**, *214*, 1081.
- (5) (a) Armbrüster, M.; Kovnir, K.; Friedrich, M.; Teschner, D.; Wowsnick, G.; Hahne, M.; Gille, P.; Szentmiklósi, L.; Feuerbacher, M.; Heggen, M.; Girgsdies, F.; Dosenthal, D.; Schlögl, R.; Grin, Yu. *Nat. Mater.* **2012**, *11*, 690. (b) Armbrüster, M.; Wowsnick, G.; Friedrich, M.; Heggen, M.; Cardoso-Gil, R. *J. Am. Chem. Soc.* **2011**, *133*, 9112. (c) Armbrüster, M.; Kovnir, K.; Behrens, M.; Teschner, D.; Grin, Yu.; Schlögl, R. *J. Am. Chem. Soc.* **2010**, *132*, 14745. (d) Li, L. D.; Zhang, B. S.; Kunkes, E.; Föttinger, K.; Armbrüster, M.; Su, D. S.; Wei, W.; Schlögl, R.; Behrens, M. *ChemCatChem* **2012**, *11*, 1764. (e) Krajčič, M.; Hafner, J. *J. Catal.* **2012**, *295*, 70. (f) Köhler, D.; Heise, M.; Baranov, A. I.; Luo, Y.; Geiger, D.; Ruck, M.; Armbrüster, M. *Chem. Mater.* **2012**, *24*, 1639.
- (6) (a) Ruiz-Martínez, J.; Fukui, Y.; Komatsu, T.; Sepúlveda-Escribano, A. *J. Catal.* **2008**, *150*, 70. (b) Rodiansono, K. S.; Hara, T.; Ichikuni, N.; Shimazu, S. *Catal. Sci. Technol.* **2012**, *2*, 2139.
- (7) (a) Ota, A.; Kunkes, E. L.; Kasatkin, I.; Groppo, E.; Ferri, D.; Poceiro, B.; Yerga, R. M. N.; Behrens, M. *J. Catal.* **2012**, *293*, 27. (b) Collins, S. E.; Delgado, J. J.; Mira, C.; Calvino, J. J.; Bernal, S.; Chiavassa, D. L.; Baltanás, M. A.; Bonivardi, A. L. *J. Catal.* **2012**, *292*, 90.
- (8) (a) Abe, H.; Matsumoto, F.; Alden, L. R.; Warren, S. C.; Abruña, H. D.; Disalvo, F. J. *J. Am. Chem. Soc.* **2008**, *130*, 5452. (b) Rivera-Casado, E.; Volpe, D. J.; Alden, L.; Lind, C.; Downie, C.; Vazquez-Alvarez, T.; Angelo, A. C. D.; Disalvo, F. J.; Abruña, H. D. *J. Am. Chem. Soc.* **2004**, *126*, 4043.
- (9) (a) Onda, A.; Komatsu, T.; Yashima, T. *J. Catal.* **2001**, *201*, 13. (b) Onda, A.; Komatsu, T.; Yashima, T. *J. Catal.* **2003**, *221*, 378.
- (10) Lekse, J. W.; Stagger, T. J.; Aitken, J. A. *Chem. Mater.* **2007**, *19*, 3601.
- (11) (a) Falbe, J.; Bahrmann, H.; Lipps, W.; Meyer, D. In *Ullmanns Encyclopedia of Industrial Chemistry*; Wiley-VCH: Weinheim, Germany, 2005; Vol. 11, p 21. (b) Corma, A.; Iborra, S.; Velty, A. *Chem. Rev.* **2007**, *107*, 2411. (c) Climent, M. J.; Corma, A.; Iborra, S. *Green Chem.* **2011**, *13*, 520.
- (12) (a) Claus, P. *Top. Catal.* **1998**, *5*, 51. (b) Gallezot, P.; Richard, D. *Catal. Rev.: Sci. Eng.* **1998**, *40*, 81. (c) Sordelli, R.; Psaro, G.; Vlaic, G.; Cepparo, A.; Recchia, S.; Dossi, C.; Fusi, A.; Zannoni, R. *J. Catal.* **1999**, *182*, 186. (d) Margitfalvi, J. L.; Vankó, G.; Borbáth, I.; Tompos, A.; Vertes, A. *J. Catal.* **2000**, *190*, 474. (e) Riguette, B. A.; Rodrigues, C. E. C.; Morales, M. A.; Saitovitch-Baggio, E.; Gengembre, L.; Payen, E.; Marques, C. M. P.; Bueno, J. M. C. *Appl. Catal., A* **2009**, *318*, 90.
- (13) (a) Aguirre, M. D. C.; Reyes, P.; Oportus, M.; Melian-Cabrera, I.; Fierro, J. L. G. *Appl. Catal., A* **2009**, *233*, 183. (b) Recchia, S.; Dossi, C.; Poli, N.; Fusi, A.; Sordelli, L.; Psaro, R. *J. Catal.* **1999**, *184*, 1.
- (14) Chen, X.; Li, M.; Guan, J. C.; Wang, X. K.; Williams, C. T.; Liang, C. H. *Ind. Eng. Chem. Res.* **2012**, *51*, 3604.
- (15) (a) Gursky, J. A.; Blough, S. D.; Luna, C.; Gomez, C.; Luevano, A. N.; Gardner, E. A. *J. Am. Chem. Soc.* **2006**, *128*, 8376. (b) Williams, G. R.; O'Hare, D. *J. Mater. Chem.* **2006**, *16*, 3065. (c) Fogg, A. M.; Rohl, A. L.; Parkinson, G. M.; O'Hare, D. *Chem. Mater.* **1999**, *11*, 1194. (d) Li, L.; Feng, Y.; Li, Y.; Zhao, W.; Shi, J. *Angew. Chem., Int. Ed.* **2009**, *48*, 5888.
- (16) (a) Liu, H. C.; Min, E. Z. *Green Chem.* **2006**, *8*, 657. (b) Goh, K. H.; Lim, T. T.; Dong, Z. L. *Water Res.* **2008**, *42*, 1343.
- (17) (a) Li, C.; Wang, L. Y.; Wei, M.; Evans, D. G.; Duan, X. *J. Mater. Chem.* **2008**, *18*, 2666. (b) He, S.; Zhang, S. T.; Lu, J.; Zhao, Y. F.; Ma, J.; Wei, M.; Evans, D. G.; Duan, X. *Chem. Commun.* **2011**, *47*, 10797. (c) Zhao, M. Q.; Zhang, Q.; Huang, J. Q.; Wei, F. *Adv. Funct. Mater.* **2012**, *22*, 675. (d) Li, C. M.; Zhou, J. Y.; Gao, W.; Zhao, J. W.; Liu, J.; Zhao, Y. F.; Wei, M.; Evans, D. G.; Duan, X. *J. Mater. Chem. A* **2013**, *1*, 5370. (e) He, S.; Li, C. M.; Chen, H.; Su, D. S.; Zhang, B. S.; Gao, X. Z.; Wang, B. Y.; Wei, M.; Evans, D. G.; Duan, X. *Chem. Mater.* **2013**, *1*, 1040.
- (18) (a) Segall, M. D.; Lindan, P. J. D.; Probert, M. J.; Pickard, J.; Hasnip, P. J.; Clark, S. J.; Payne, M. C. *J. Phys.: Condens. Matter* **2002**, *14*, 2717. (b) Delley, B. *J. Chem. Phys.* **1990**, *92*, 508.
- (19) (a) Hellner, E. Z. *Metallkd.* **1950**, *41*, 401. (b) Bhattacharya, B.; Masson, D. B. *Mater. Sci. Eng.* **1976**, *22*, 133. (c) Ruhl, R. C.; Giessen, B. C.; Cohen, M.; Grant, N. J. *Mater. Sci. Eng.* **1967**, *2*, 314. (d) Hellner, E. Z. *Metallkd.* **1950**, *41*, 177.
- (20) Sideris, P. J.; Nielsen, U. G.; Gan, Z.; Grey, C. P. *Science* **2008**, *321*, 113.
- (21) Brindley, G. W.; Kikkawa, S. A. *Am. Mineral.* **1979**, *64*, 836.
- (22) (a) Corma, A.; Iborra, S.; Velty, A. *Chem. Rev.* **2007**, *107*, 2411. (b) Climent, M. J.; Corma, A.; Iborra, S. *Green Chem.* **2011**, *13*, 520. (c) Herbois, R.; Noel, S.; Leger, B.; Bai, L.; Roucoux, A.; Monflier, E.; Ponchel, A. *Chem. Commun.* **2012**, *48*, 3451.
- (23) Wu, J.; Shen, Y. M.; Liu, C. H.; Wang, H. B.; Geng, C. J.; Zhang, Z. X. *Catal. Commun.* **2005**, *6*, 633.
- (24) Sharma, R. V.; Das, U.; Sammynaiken, R.; Dalai, A. K. *Appl. Catal., A* **2013**, *454*, 127.
- (25) Alayoglu, S.; Zavalij, P.; Eichhorn, B.; Wang, Q.; Frenkel, A. I.; Chupas, P. *ACS Nano* **2012**, *3*, 3127.
- (26) Zhang, J. L.; Zhang, M.; Han, Y.; Li, W.; Meng, X. K.; Zong, B. N. *J. Phys. Chem. C* **2008**, *112*, 19506.
- (27) (a) Osswald, J.; Giedigkeit, R.; Jentoft, R. E.; Armbrüster, M.; Girgsdies, F.; Kovnir, K.; Ressler, T.; Grin, Yu.; Schlögl, R. *J. Catal.* **2008**, *258*, 210. (b) Osswald, J.; Kovnir, K.; Armbrüster, M.; Giedigkeit, R.; Jentoft, R. E.; Wild, U.; Grin, Yu.; Schlögl, R. *J. Catal.* **2008**, *258*, 219.
- (28) Delbecq, F.; Sautet, P. *J. Catal.* **1995**, *152*, 217.
- (29) (a) Jin, Y. M.; Datye, A. K.; Rightor, E.; Gulotty, R.; Waterman, W.; Smith, M.; Holbrook, M.; Maj, J.; Blackson, J. *J. Catal.* **2001**, *203*, 292. (b) Kang, J. H.; Shin, E. W.; Kim, W. J.; Park, J. D.; Mon, S. H. *J. Catal.* **2002**, *208*, 310. (c) Medlin, J. W.; Allendorf, M. D. *J. Phys. Chem. B* **2003**, *107*, 217.
- (30) Hsu, L.-S.; Nesvizhskii, A. I. *J. Phys. Chem. Solids* **2001**, *32*, 1103.